Physics of Plasmas

Mapping of the HIDRA stellarator magnetic flux surfaces

Cite as: Phys. Plasmas **26**, 092503 (2019); https://doi.org/10.1063/1.5100744
Submitted: 19 April 2019 . Accepted: 19 August 2019 . Published Online: 06 September 2019

Rabel Rizkallah, Steven Marcinko, Davide Curreli, Matthew S. Parsons, Nathan Bartlett, Raanan Gluck, Andrew Shone, and Daniel Andruczyk

View Online Export Citation CrossMark

ARTICLES YOU MAY BE INTERESTED IN

Poloidally localized edge density fluctuation with applied and spontaneous 3-D fields in experimental advanced superconducting tokamak (EAST)
Physics of Plasmas **26**, 092504 (2019); https://doi.org/10.1063/1.5119020

Long-lived predator-prey dynamics in the pedestal of near-zero torque high performance DIII-D plasmas
Physics of Plasmas **26**, 092501 (2019); https://doi.org/10.1063/1.5097143

Arc discharges during disruptions in the T-10 tokamak
Physics of Plasmas **26**, 092505 (2019); https://doi.org/10.1063/1.5102112

© 2019 Author(s).

Physics of Plasmas ARTICLE scitation.org/journal/php

Mapping of the HIDRA stellarator magnetic flux surfaces

Cite as: Phys. Plasmas **26**, 092503 (2019); doi: 10.1063/1.5100744
Submitted: 19 April 2019 · Accepted: 19 August 2019 ·
Published Online: 6 September 2019

View Online Export Citation CrossMark

Rabel Rizkallah,[a] Steven Marcinko, Davide Curreli, Matthew S. Parsons, Nathan Bartlett, Raanan Gluck, Andrew Shone, and Daniel Andruczyk

AFFILIATIONS

Center for Plasma-Material Interactions, Department of Nuclear, Plasma and Radiological Engineering, University of Illinois at Urbana-Champaign, Urbana, Illinois 61801, USA

[a]Electronic mail: rabeler2@illinois.edu

ABSTRACT

The Hybrid Illinois Device for Research and Applications (HIDRA) is a classical stellarator designed for conducting plasma material interaction experiments and developing novel Plasma Facing Components (PFCs). Notably, the testing of two open-channel liquid lithium PFCs is imminent. Determining the shape of the plasma and its magnetic structure inside HIDRA is essential to carry out these tests. For this, electron traces were captured to build up the images of the HIDRA magnetic flux surfaces for several magnetic configurations, following the same procedure previously employed on the WEGA stellarator coupling an electron gun with a fluorescent detector. The FIELDLINES code has then been used to generate computational surfaces matching the experimental results. The obtained surfaces were found to be subject to a similar $n = 1$ error field as the one observed on WEGA, suggesting that the origin of this error field is inherent to the HIDRA vacuum vessel. Also, the effect of adding a vertical field was investigated, demonstrating the ability to radially shift the magnetic axis and move to a regime free of low-order rational resonances. This additional control over the HIDRA plasma and magnetic structure allows more freedom in setting up the PFC tests in the limiter and divertor regions.

Published under license by AIP Publishing. https://doi.org/10.1063/1.5100744

I. INTRODUCTION

The Hybrid Illinois Device for Research and Applications (HIDRA) is an $l = 2$, classical stellarator with a fivefold toroidal symmetry operated at the Center for Plasma-Material Interactions (CPMI) at the University of Illinois at Urbana-Champaign (UIUC).[1] It is a midsized device with a major radius of $R_0 = 72$ cm and a minor radius of $a = 19$ cm. Before arriving at CPMI, HIDRA was run under the name WEGA at the Max-Planck Institut für Plasmaphysik (IPP) in Greifswald, Germany. Taking advantage of its steady-state capabilities, HIDRA is meant to be used to run Plasma Material Interaction (PMI) experiments, with a major focus on testing and developing liquid lithium Plasma Facing Components (PFCs).[2] Two such PFC concepts are of special interest: The Liquid-Metal Infused Trenches (LiMIT)[3,4] developed at CPMI which takes advantage of the thermoelectric magnetohydrodynamic (TEMHD) effect[5] and the Flowing Liquid Lithium (FLiLi)[6,7] developed at the Princeton Plasma Physics Laboratory (PPPL). Both designs are plate-like components over which flows a thin layer of liquid lithium desired to be under 1 mm thick. The lithium creates the interface between the PFC and the plasma in an attempt to avoid damage to the plates.[3] While the initial tests will use LiMIT and FLiLi as limiters, the experiments will move toward testing these concepts as plasma divertors. HIDRA is also getting an additional material testing module, the HIDRA-Material Analysis Tool (HIDRA-MAT), designed to expose samples to the plasma and test the various interactions different materials may exhibit, which will further enhance the PFC research and development capabilities of HIDRA.[1] Distributed around the vacuum vessel are 100 ports of seven different sizes and port positions, which in the descending port diameter are labeled as A, B, C, Z, D, E, and F ports. These ports are used to install the required pumps to achieve vacuum and necessary diagnostics to conduct experiments on HIDRA. A schematic of the various ports is shown in Fig. 1.

Understanding the shape and different magnetic configurations of the HIDRA plasma is crucial to run desired PFC tests. A complete mapping of the magnetic topology of the device would help in determining what radial position and plate angle to go with. Due to the accessibility of the ports on HIDRA and the required space to be taken by the PFC support structure and attached diagnostics, only a few ports are feasible to be used to mount the LiMIT and FLiLi plates. The designated candidate ports are A-ports for the limiter configuration and E-ports for the divertor configuration, both at toroidal angles of $\varphi = 144°$ and $\varphi = 216°$. Determining the magnetic topology at one of

Published under license by AIP Publishing

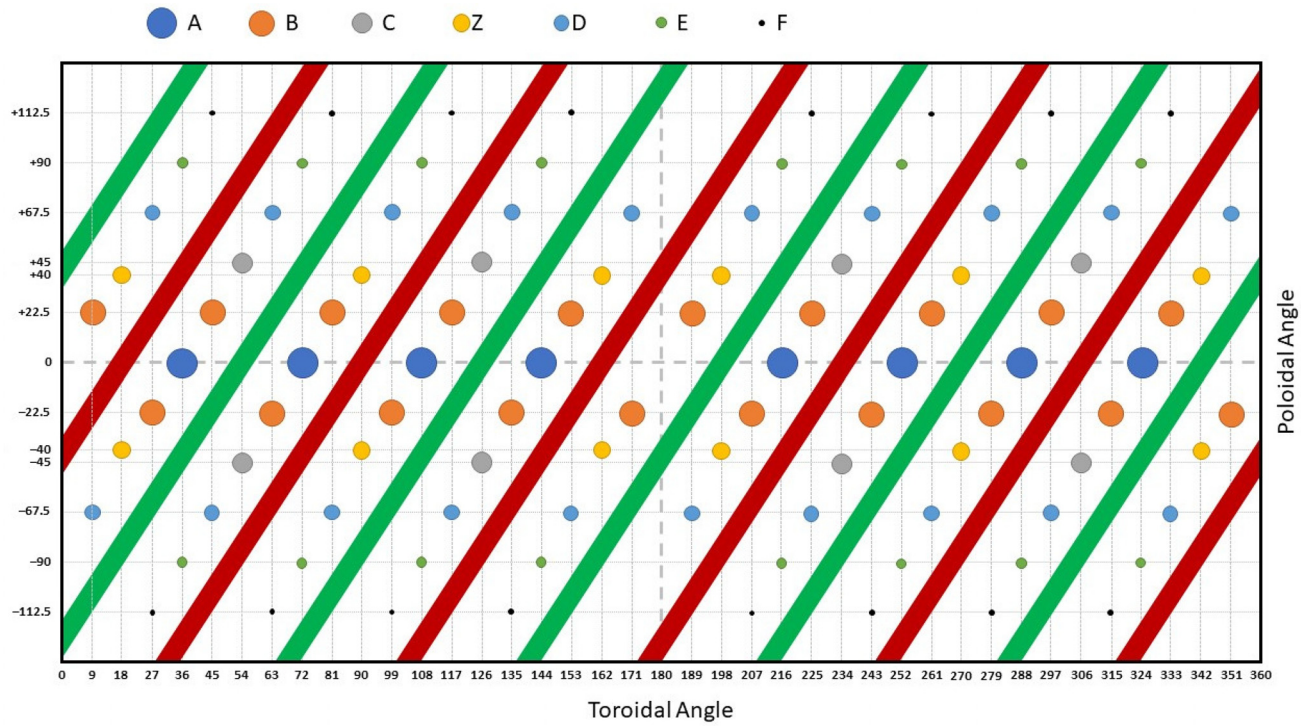

FIG. 1. Schematic of the different ports present around HIDRA. The largest A-ports are located at the midplane, with a diameter of 92 mm. The smaller E-ports, with a diameter of 50 mm, are located at a poloidal angle of $\pm 90^\circ$ at the same toroidal angles where the A-ports are.

the ports is enough because of the fivefold toroidal symmetry of the device. Moreover, measurements were done with the addition of a vertical field to verify and observe its effects. It was previously shown on WEGA that in addition to the closed and nested flux surfaces, some non-natural islands arise at low order rational rotational transform values because of the existence of undesired magnetic error fields.[8] The principal error field concerned with these islands was of the order of $n = 1$ with n being the toroidal mode number. The WEGA experiments also showed that because the shear is sufficiently small, the addition of a vertical field allows us to find regions without the $n = 1$ islands close to the desired rotational transform. In addition, the vertical field allows radial shifting of the magnetic axis both inward and outward. This is a very useful option for the PFC experiments planned on HIDRA, as it increases the control over the plasma and gives more freedom in setting up the experimental apparatus.

The magnetic surfaces were experimentally measured at the two toroidal positions of the candidate ports for running the LiMIT and FLiLi tests for the rotational transforms of $\approx 1/3$, 1/4, and 1/5, in a low-field regime with an on-axis magnetic field of $B_0 = 70$ mT. It was previously shown that the same magnetic topology exists regardless of the magnitude of the on-axis magnetic field, for the same rotational transform.[8] Measurements were performed with no vertical field at first and then with the addition of a vertical field. The experimental measurements are reported here and compared to computational results, in an attempt to map the HIDRA plasma and further understand the origin of the error field.

The FIELDLINES[9,10] code from the STELLOPT code suite, a stability optimization code for stellarators,[11,12] was used to computationally generate the vacuum magnetic surfaces and compare them to the experimentally obtained ones. The code can also incorporate an error field that was chosen identical to the one reported from the WEGA experiments in an initial attempt to reproduce the HIDRA error field. After failing to obtain a proper match with the experimental images following this approach, the coil geometry file of HIDRA was modified to include a physical misalignment between the toroidal coils and the helix, allowing for a much better representation of the observed error field. When comparing the experimental magnetic flux surfaces with the computational ones, matching them together would help determine whether the HIDRA error field is similar to the one witnessed on WEGA, giving some insight into the origin of this field.

II. OBTAINING THE FLUX SURFACES

A. Experimental procedure

To measure the magnetic surfaces, the electron gun technique[13] previously employed on WEGA[14,15] was used. The electron gun consists of a tungsten filament attached to a manipulator arm that can be displaced radially across the vacuum vessel along the midplane. The filament is covered by a grounded cap having a hole of ≈ 8 mm through which the electrons can escape parallel to the magnetic field lines. For this, an accelerating voltage of 300 V was applied between the filament and the cap, with the filament set at a negative potential. The free electrons emitted from the filament follow the magnetic lines when going around the vacuum vessel as visualized in Fig. 2.

Published under license by AIP Publishing

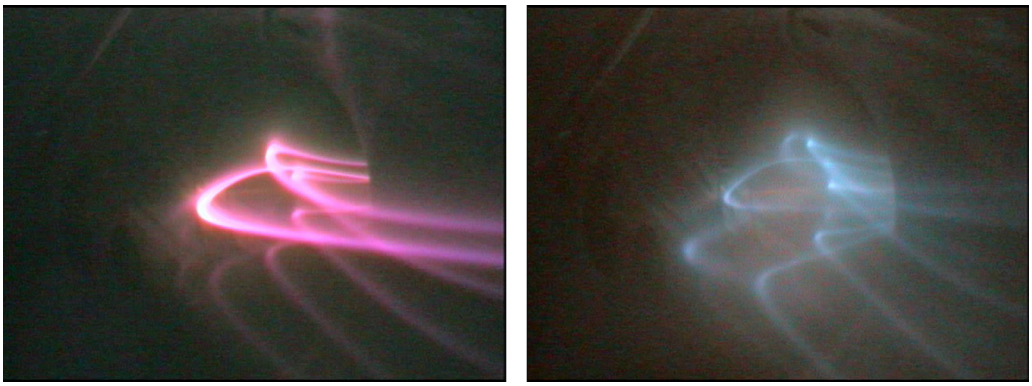

FIG. 2. Electron traces along magnetic lines in nitrogen (left) and helium (right) background gases.

The electron trajectories slightly differ from the magnetic field lines because of drifts. However, the change is very small[13] and allows good approximation to the magnetic flux surfaces as further discussed in Sec. II B. For a fixed radial position of the filament, the electron traces interacted with a rod covered with a (ZnO:Zn) fluorescent powder and mounted on an A-port where it swept the whole poloidal cross section. The powder causes the rod to fluoresce when intersecting the path of the free electrons. Two toroidal positions of the rod were used to perform the measurements, at $\varphi = 144°$ and $\varphi = 216°$ with the electron gun positioned at $\varphi = 72°$. A long-time integrating Starlight Xpress HX916 CCD-camera captured the electron traces on the fluorescent rod, generating one image per fixed radial position of the filament, such as the ones shown in Fig. 3. The camera and sweeping rod were separated toroidally by 36° for both locations of the rod. Three light emitting diodes (LEDs) lights were also installed inside the vacuum vessel at the toroidal position where measurements were being performed. Two of these LEDs were installed along the vertical diameter of the HIDRA vessel, 5 cm away from the top and bottom walls, respectively. The third LED was positioned along the midplane, 5 mm away from the wall on the high-field side. These reference points were used to scale the measured location of the magnetic axis and relate the measurements to the physical location and size of the magnetic flux surfaces. After filtering the individual images, the magnetic surfaces were obtained by superimposing them, for the same magnetic configuration. This procedure was used to build magnetic surfaces for the rotational transforms of ≈1/3, 1/4, and 1/5, with and without a vertical field. The composite images are presented in Fig. 4 with no vertical field, and in Figs. 6 and 7 after the addition of a vertical field. The toroidal current was kept constant for all the performed measurements, at $I_T = 486$ A corresponding to an on-axis magnetic field of $B_0 = 70$ mT, given for HIDRA by Eq. (1). During this experimental campaign, the input/output connections from the rectifiers to the toroidal coils were reversed and kept as such throughout the experimental measurements. The toroidal current was therefore flowing in the negative conventional direction through the coils, resulting in flipped magnetic flux surfaces when compared to the images coming from the past WEGA measurements.

$$B_0[\mathrm{T}] = 1.44 \times 10^{-4}\, I_T[\mathrm{A}]. \tag{1}$$

The different magnetic configurations were obtained by controlling the helical current. The rotational transform for stellarators is given by Eq. (2),[16] where l is the poloidal periodicity, N is the toroidal symmetry number, R_0 and a are the major and minor radii of the device, respectively, B_h and B_0 are the helical and toroidal magnetic fields, respectively, and r_0 is the distance of a point in space from the magnetic axis. Plugging in the HIDRA parameters in Eq. (2) with $l = 2$ and $N = 5$ reduces the expression to the simple form of Eq. (3)

$$\iota = \frac{\iota}{2\pi} = \frac{l-1}{N}\left(\frac{R_0 B_h}{a B_0}\right)^2 \left(\frac{r_0}{a}\right)^{2l-4}, \tag{2}$$

$$\iota \approx 0.1\left(\frac{I_H}{I_T}\right)^2. \tag{3}$$

Hence, only the ratio of the helical to toroidal currents is needed to obtain a desired rotational transform profile. Because the rotational transform is a dimensionless ratio, the magnetic topology is independent of the on-axis field strength and can be achieved in both high-field and low-field regimes. However, the $1/m$ rational resonance, with m being the poloidal mode number, is only reached in a small region of the magnetic flux surface as the rotational transform varies radially along the magnetic surfaces. This is further discussed in Sec. III C with rotational transform profiles shown in Fig. 9 for different magnetic configurations. Table I reports the helical and toroidal currents used for different measurements performed. These current values were initially thought to make the non-natural islands fall into the visible spatial range of the camera. Each of the three magnetic configurations was run with the vertical field currents of 0, +12, and −12 amperes.

B. Interpretation of the measurement data

A distinction should be made between the luminescent traces from the electron detector and the magnetic field lines. Two effects contribute to making the drift orbit of the electrons not coinciding with the magnetic field lines. First, the gyration creates a deviation r_G of one Larmor radius[17] according to

$$r_G = \frac{\|\vec{p}\|}{eB} \times \sin\alpha, \tag{4}$$

where $\vec{p}$ is the momentum, e the fundamental charge, B the magnetic induction, and α the pitch angle between $\vec{p}$ and magnetic field $\vec{B}$.

Published under license by AIP Publishing

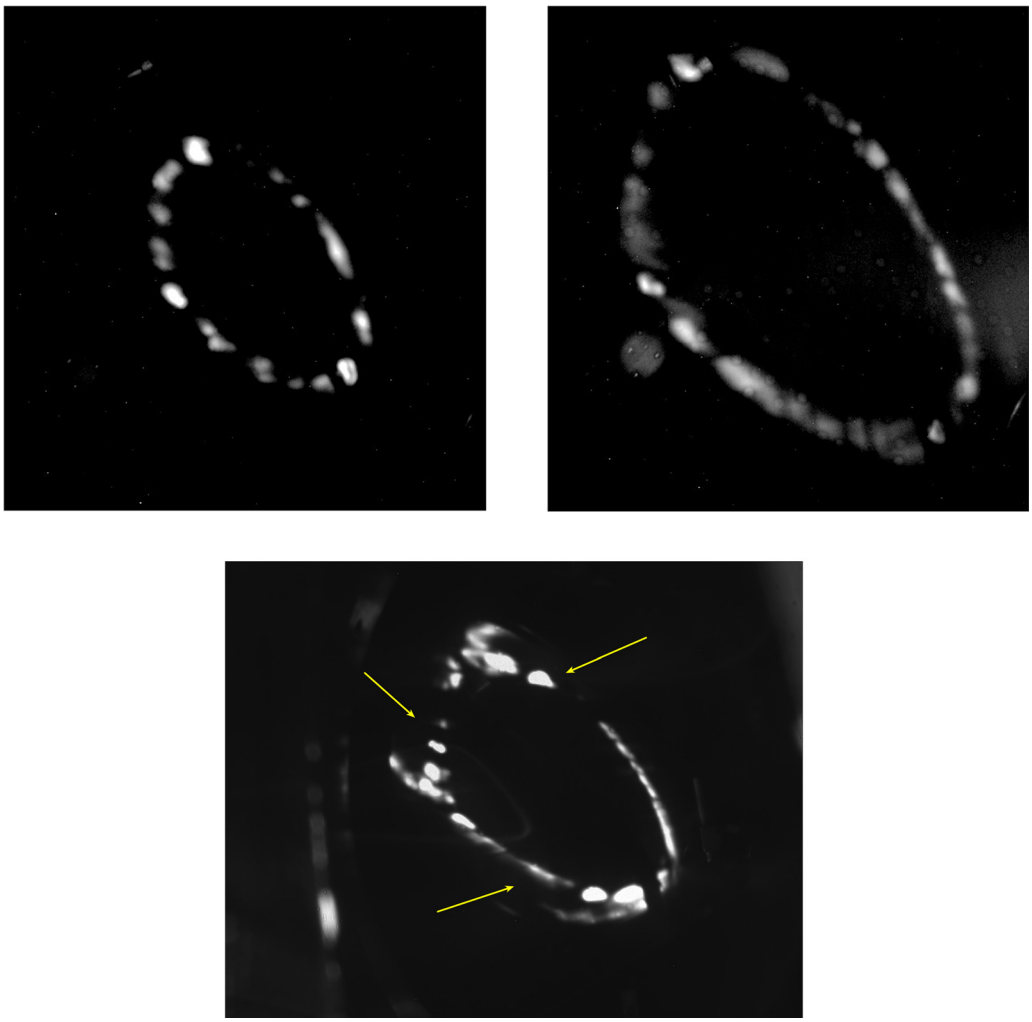

FIG. 3. Electron traces captured by using the CCD camera on the fluorescent detector for $\iota \approx 1/3$ with the electron gun filament at $R = 73$ cm (top left), $R = 75$ cm (top right), and $R = 62$ cm (bottom). The arrows point at the location of the non-natural islands which are just being reached in the bottom image. Note that the images are inverted and not yet filtered.

The heated tungsten filament creates a Maxwellian population of electrons, the velocity of which can be approximated to the thermal speed v_{th} given in Eq. (5), where k_B is the Boltzmann constant, T_e the electron temperature, and m_e the electron mass. The geometry of the cap and position of the tungsten filament also limits the angle α to a maximum value of $\approx 22°$

$$v_{th} = \sqrt{\frac{2k_B T_e}{\pi m_e}}. \tag{5}$$

With the on-axis magnetic field strength at 70 mT and $k_B T_e = 300$ eV, Eq. (4) gives a deviation of $r_G \leq 0.3$ mm which is negligible. Second, drift velocities are generated by the curvature and gradient of the magnetic field. These are given by Eqs. (6) and (7), respectively,[18] where R_c is the radius of curvature, $v_{||}$ is the component of the electron velocity parallel to $\vec{B}$, and $v_\perp$ is the component perpendicular to $\vec{B}$

$$\mathbf{v_R} = \frac{m_e v_{||}^2}{e\mathbf{B}^2} \frac{\mathbf{R}_c \times \mathbf{B}}{\mathbf{R}_c^2}, \tag{6}$$

$$\mathbf{v}_{\nabla \mathbf{B}} = -\frac{1}{2} \frac{m_e v_\perp^2}{eB} \frac{\mathbf{B} \times \nabla \mathbf{B}}{\mathbf{B}^2}. \tag{7}$$

These drifts add up resulting in an overall drift velocity $\mathbf{v_D}$. Assuming a $1/R$ dependence for the magnetic field, Eq. (7) can be written as

$$\mathbf{v}_{\nabla \mathbf{B}} = \frac{1}{2} \frac{m_e v_\perp^2}{e} \frac{\mathbf{R}_c \times \mathbf{B}}{\mathbf{R}_c^2 \mathbf{B}^2}. \tag{8}$$

Adding Eq. (8) to Eq. (6) leads to the total $\mathbf{v}_D$ drift in a curved vacuum field

$$\mathbf{v}_D = \frac{m_e}{e} \frac{\mathbf{R}_c \times \mathbf{B}}{\mathbf{R}_c^2 \mathbf{B}^2} \left(v_{||}^2 + \frac{1}{2} v_\perp^2 \right). \tag{9}$$

Published under license by AIP Publishing

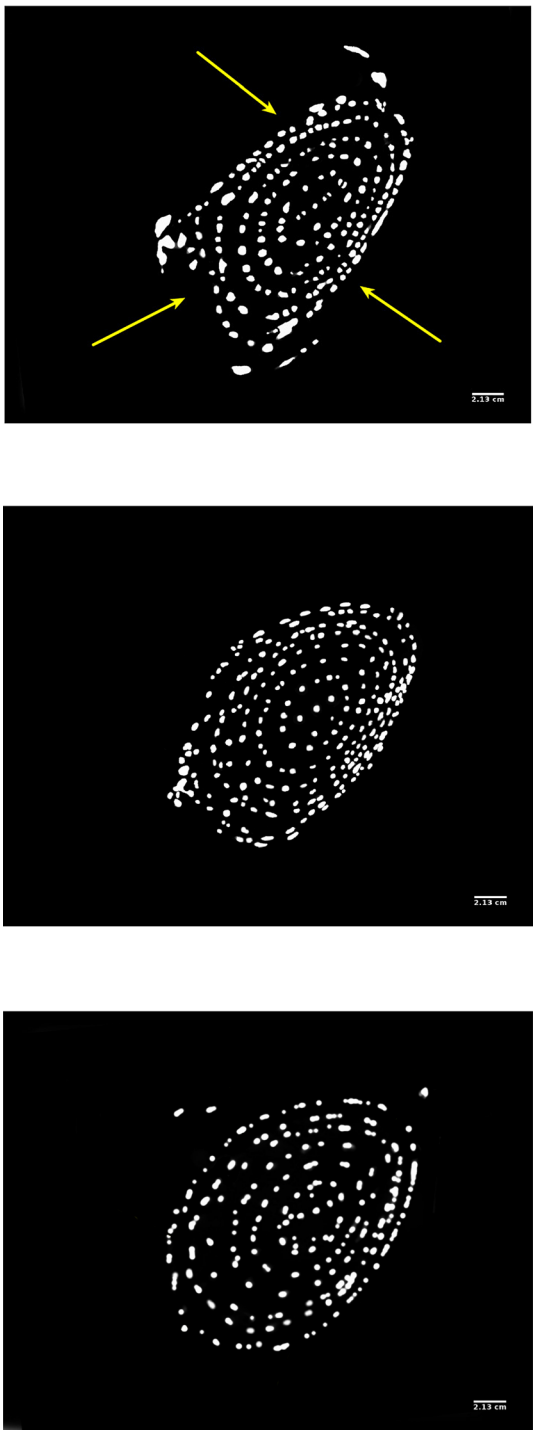

FIG. 4. Experimentally measured magnetic flux surfaces for the rotational transform values of ≈1/3 (top), ≈1/4 (middle), and ≈1/5 (bottom) with no vertical field. The arrows in the top image point at the non-natural islands starting to form, whereas the flattened magnetic surfaces at the end of the measured domain in the other two images indicate that the magnetic islands are present just outside of the last measured magnetic surface.

TABLE I. Toroidal and helical currents used for the experimental measurements of different magnetic configurations.

ι	I_T (A)	I_H (A)
≈1/3	486	900
≈1/4	486	790
≈1/5	486	710

With $B_0 = 70\,\text{mT}$, $R_c = R_0 = 72\,\text{cm}$, $v_{\|} = v_{th}\cos\alpha$, and $v_{\perp} = v_{th}\sin\alpha$, a total drift velocity can be found. This drift displaces the electron path vertically from the field line, while the particle is orbiting in the upper (or lower) half of the stellarator.[13] In the other half of the machine, and for the same orbiting time t_o, the drift path returns to the field line. To obtain the maximum resulting displacement, a constant drift $r_D = \|\mathbf{v}_D\| \times t_o$ can be assumed. For a 1/4 rotational transform, two full toroidal transits are necessary for a field line to make half of a poloidal turn. This corresponds to an orbiting time of $t_o \approx 1.5 \times 10^{-6}$ s and a drift displacement of $r_D \leq 5.5\,\text{mm}$. This drift drops to $r_D \leq 4\,\text{mm}$ for a 1/3 rotational transform and goes up to $r_D \leq 6.8\,\text{mm}$ for $\iota = 1/5$. These computed values of r_D are exaggerated by the assumption that the drift is constant over the orbit time t_o. They however give an estimate of the drift scale which is quite low. Hence, even though the electron trajectories do not follow the field lines exactly, their traces on the fluorescing rod are close enough to approximate the magnetic flux surfaces.

C. Computational procedure

Generating the computational images was done through the FIELDLINES code. 161 seed points on the midplane between $R = 60\,\text{cm}$ and $R = 76\,\text{cm}$, separated by 1 mm, were chosen as the initial generators to follow the field lines. After integrating the field lines from this initial set for 1000 toroidal transits around the vacuum vessel, a Poincaré section at the $\varphi = 216°$ plane was obtained. The resulting section is identical to the one on the $\varphi = 144°$ poloidal plane because of the toroidal symmetry of HIDRA. Moreover, for the sake of comparison with the WEGA results, the same $n = 1$ error field reported from the WEGA experiments[8,14] was added to FIELDLINES. Also, the toroidal current was inputted as negative 486 A to match its physical direction through the toroidal field coils resulting from the reversed input/output connections. However, simply adding the $n = 1$ error field with a perfectly symmetric coil geometry file led to the computational results displaying different dimensions of the magnetic surfaces and much smaller magnetic islands than the ones hinted at in the experimental images. Hence, to address this issue, the coil geometry file was itself modified to introduce a horizontal offset between the vertical axis of the toroidal and helical field coils. Such an offset of the order of ≈3 mm was suggested by the WEGA team to be the origin of the error field.[8] One particular feature of HIDRA allows for its vacuum vessel to split into two half-tori. The horizontal offset between the toroidal and helical coils was applied to the helix, perpendicular to the poloidal plane where the two half-tori separate. Several positions of the helix were tested, from a uniform shift of the whole helix starting at 1 and up to 5 mm to different shifts of the helical packets on each of the two half-tori in the same and along opposite directions. The FIELDLINES output corresponding to each of the tested offsets was

Published under license by AIP Publishing

compared to the experimentally measured magnetic surfaces. Unfortunately, since not enough magnetic features appeared in the measured images, determining which coil model best represents the physical system was not trivial. In general, a uniform shift of 4 mm of the helix resulted in computational magnetic surfaces satisfactorily close to the experimentally measured surfaces for the different magnetic configurations tested. Similar dimensions of the overall magnetic flux surfaces and radial locations of the islands can be observed in both the experimental and computational images with such an offset. This coil model was therefore adopted to carry out the computational generation of the magnetic surfaces.

After the initial FIELDLINES run, processing the coordinates of the magnetic surfaces in the Poincaré section allowed for the location of the magnetic axis and the last closed flux surface (LCFS) to be estimated. To obtain smooth and closed magnetic surfaces, the ones within the LCFS were splined with the *splrev* and *splrep* Python libraries and filtered with a Savitzky-Golay filter. For this, the global (R, Z) cylindrical coordinates of the magnetic lines were transformed to local polar (r, θ) coordinates with the magnetic axis as the new origin, giving a function-like distribution of r with respect to θ. The splining and filtering were applied to the coordinates of each magnetic line in the new local frame. The splining was efficient at smoothing the magnetic surfaces outside the island regions, whereas the filtering achieved this when going through the islands. The splined and filtered magnetic surfaces were then traced back into FIELDLINES. In the second run of FIELDLINES, only the generators with a radial coordinate greater than the approximated magnetic axis radial coordinate were kept so that each magnetic surface is traced only once. The upper bound of $R = 76$ cm was increased so that the full confined region was properly traced. From the new output, the magnetic axis was found, and a Poincaré section at the A-port of interest was generated, as well as a radial rotational transform profile.

This routine was repeated for every magnetic configuration of Table I, with and without the addition of a vertical field. For each case, the exact location of the magnetic axis was determined in the global (R, Z) coordinate system. The results are shown in Table II with no vertical field. All three magnetic configurations exhibit the same radial position of the magnetic axis located very close to the midplane at $R \approx 70.5$ cm. Following the addition of a vertical field, the position of the magnetic axis changes, as is presented in Table III for different magnetic configurations.

III. RESULTS AND DISCUSSION

A. Comparison of the measured and computational magnetic flux surfaces with no vertical field

The Poincaré sections obtained from the FIELDLINES runs present considerably greater resolution and precision than the experimental images. This is due to the limitation of the experimental setup used and difficulty in filtering out the background noise coming from outgassing from the camera shots. By reducing the number of generators used to carry out the magnetic line tracing, less precise images were obtained, making for better comparison with the experimental measurements. However, the higher precision is desirable to better resolve the magnetic features. Therefore, the full resolution of the computational Poincaré surfaces was retained. Keeping that in mind, the comparison between the experimental and computational flux surfaces is done from a qualitative perspective. As such, a good match between the two was observed, from the position of the magnetic axis and location of the magnetic islands to the overall shape and size of the magnetic flux surfaces. The measured magnetic surfaces were found to be comparable to those measured on WEGA for similar magnetic configurations. The experimental images obtained from building up the individual electron traces for the rotational transform values of ≈1/3, 1/4, and 1/5 with no vertical field are shown in Fig. 4, with the corresponding computational Poincaré sections shown in Fig. 5. Among the experimental images, only the $\iota \approx 1/3$ case displayed non-natural islands starting to form at the last measured magnetic surface. The other magnetic configurations did not display such islands but did exhibit flattened magnetic surfaces in the outer regions, an indicator that the non-natural islands were present outside the measured domain. Similar looking magnetic surfaces to the ones of Fig. 4 can be observed in Fig. 5 before reaching the magnetic islands. The location of the non-natural islands for $\iota \approx 1/3$ is in good agreement between Figs. 4 and 5, and so are the shape and position of the deformed magnetic surfaces before reaching the islands for the other magnetic configurations.

The similarity between the experimental and computational magnetic flux surfaces shows that the FIELDLINES parameters nicely reproduced the system at hand. This suggests that the computational coil model successfully emulated the error field experienced by the electron beam technique. The dimensions of the non-natural islands for the various magnetic configurations were bigger than those previously observed on WEGA. Because the disassembly and reassembly HIDRA went through when moving from Greifswald to CPMI, it was expected that a slightly different error field may be encountered, in particular if the theory that the origin of the error field comes from the physical machine itself holds. The results from this campaign seem to back this up and confirm that engineering imperfections and slight misalignments between the HIDRA magnetic field coils are breaking the stellarator symmetry and generating the error field.

All three of the magnetic configurations studied gave the same location for the magnetic axis as already reported in Table II, which is

TABLE II. Computationally determined positions of the magnetic axis for different rotational transforms at $\varphi = 144°$ (or $\varphi = 216°$) with no vertical field.

ι	R (cm)	Z (mm)
≈1/3	70.5044	1.0192
≈1/4	70.4971	6.8773×10^{-1}
≈1/5	70.4927	5.0402×10^{-1}

TABLE III. Computationally determined positions of the magnetic axis at $\varphi = 144°$ (or $\varphi = 216°$) with the addition of a vertical field.

ι	$I_V = +12$ A	$I_V = -12$ A
≈1/3	$R = 68.9702$ cm $Z = -2.6324$ mm	$R = 71.8355$ cm $Z = 4.5489$ mm
≈1/4	$R = 68.4711$ cm $Z = -3.4346$ mm	$R = 72.1832$ cm $Z = 4.5917$ mm
≈1/5	$R = 67.9359$ cm $Z = -4.0736$ mm	$R = 72.5317$ cm $Z = 4.7632$ mm

Published under license by AIP Publishing

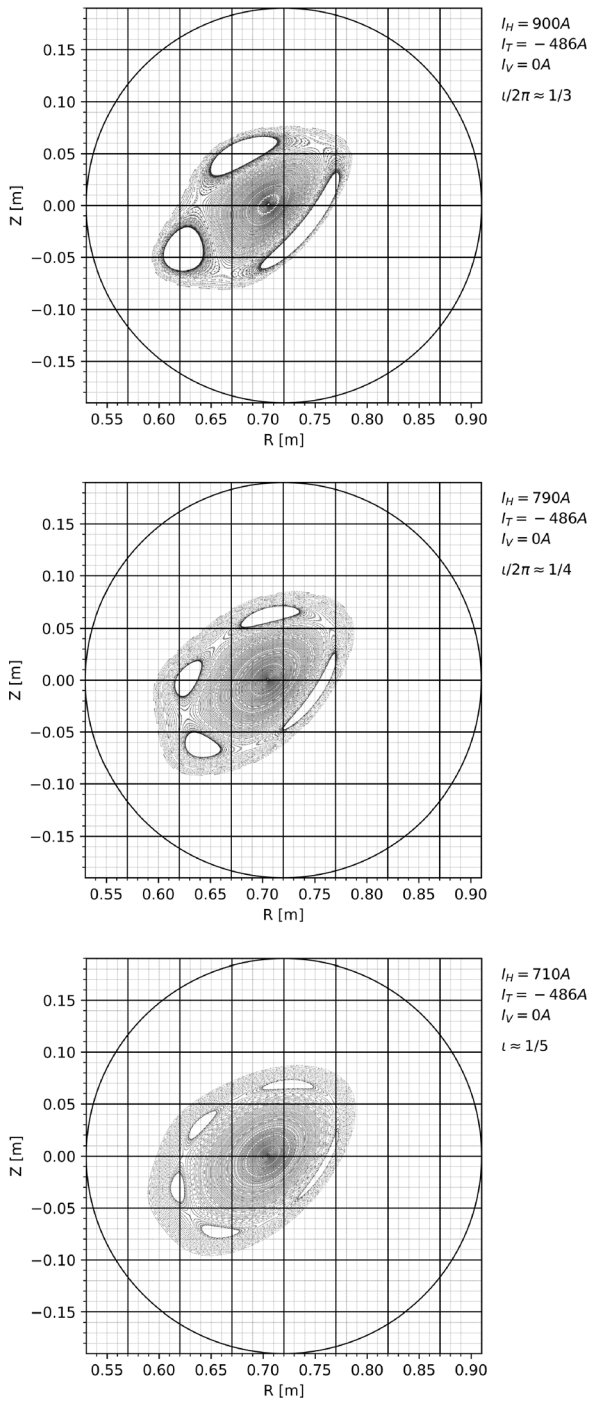

FIG. 5. Poincaré sections obtained through FIELDLINES for the rotational transforms of ≈1/3 (top), ≈1/4 (middle), and ≈1/5 (bottom) with no vertical field.

radially 20.5 cm away from the wall on the low-field side, from where the limiters and HIDRA-MAT samples will be exposed to the plasma and tested. Finding the location of the magnetic axis from the experimental images gave an estimated position on the midplane at $R \approx 71.2$ cm which is slightly larger than the computational results. The analysis of this difference is shown in Sec. III B, after presenting further experimental measurements.

B. Comparison of the measured and computational magnetic flux surfaces with the vertical field

Applying a vertical field was achieved by running +12 A and −12 A currents in the vertical coils. As expected, this resulted in a regime with no $n = 1$ non-natural islands and shifted the magnetic axis position.[8] However, the experimentally observed shift of the magnetic axis was not as important as expected based on the previous WEGA experiments and the computational results. For a +12 A current through the vertical field coils, the radial shifts of the magnetic axis toward the high-field side of ≈1.2 cm and ≈1.6 cm were measured from the experimental images for the magnetic configurations of $\iota \approx 1/3$ and $\iota \approx 1/4$, respectively. The computational results on the other hand predict the shifts of ≈1.5 cm and ≈2 cm in the same direction, in agreement with the measurements from the WEGA campaigns for comparable rotational transforms. The experimental magnetic flux surfaces and the corresponding computational Poincaré sections with a positive vertical field coil current are shown in Fig. 6 for the rotational transforms of ≈1/3 and ≈1/4. The new radial and horizontal positions of the magnetic axis with the addition of a vertical field as calculated through FIELDLINES are given in Table III.

The reason for the discrepancy between the experimentally measured magnetic axis shifts and the computational ones was first thought to be a misalignment of the vertical field coils which was present during the experimental measurements. The top vertical coil was inclined toward the vacuum vessel by about 7 cm at the $\varphi = 90°$ toroidal position. However, adding this misalignment to the FIELDLINES code did not seem to affect the shift of the magnetic axis. With misaligned vertical coils, the FIELDINES calculations gave the radial shifts of the magnetic axis of 68.9168 cm and 68.4099 cm for the rotational transforms of ≈1/3 and ≈1/4, respectively. These are very close to the values of Table III for perfectly aligned vertical coils. The horizontal shift is similarly barely affected with a 0.1 mm difference between the aligned and misaligned coil cases. The trend observed from the computational radial shifts of the magnetic axis shows that it increases by 0.5 cm from $\iota \approx 1/3$ to $\iota \approx 1/4$ and then again from $\iota \approx 1/4$ to $\iota \approx 1/5$. The radial shift difference between the 1/3 and 1/4 rotational transforms from the experimental images is slightly below that at ≈0.4 cm. A possible reason for the difference between the observed magnetic axis shifts and computed ones could be the particle drifts discussed in Sec. II B. The amount by which the experimental and computational entities differ is small enough to be of the same scale as the drifts felt by the electrons. Combined with the somewhat poor experimental resolution, this can easily make up for a few millimeters when determining the shift of the magnetic axis. It can also be the reason behind the measured location of the magnetic axis with no vertical field which was off by approximately 7 mm.

Another possible factor which may have affected the measurements is the used CCD camera which probably was not looking perpendicular to the pivot plane of the rod. This is somehow hinted at in the experimental images in Figs. 4, 6, and 7 by the higher density of electron traces on the low-field side as compared to the high-field side. The higher density of traces can be due to the compression of the magnetic lines, but the observed images displayed lines on top of one

Published under license by AIP Publishing

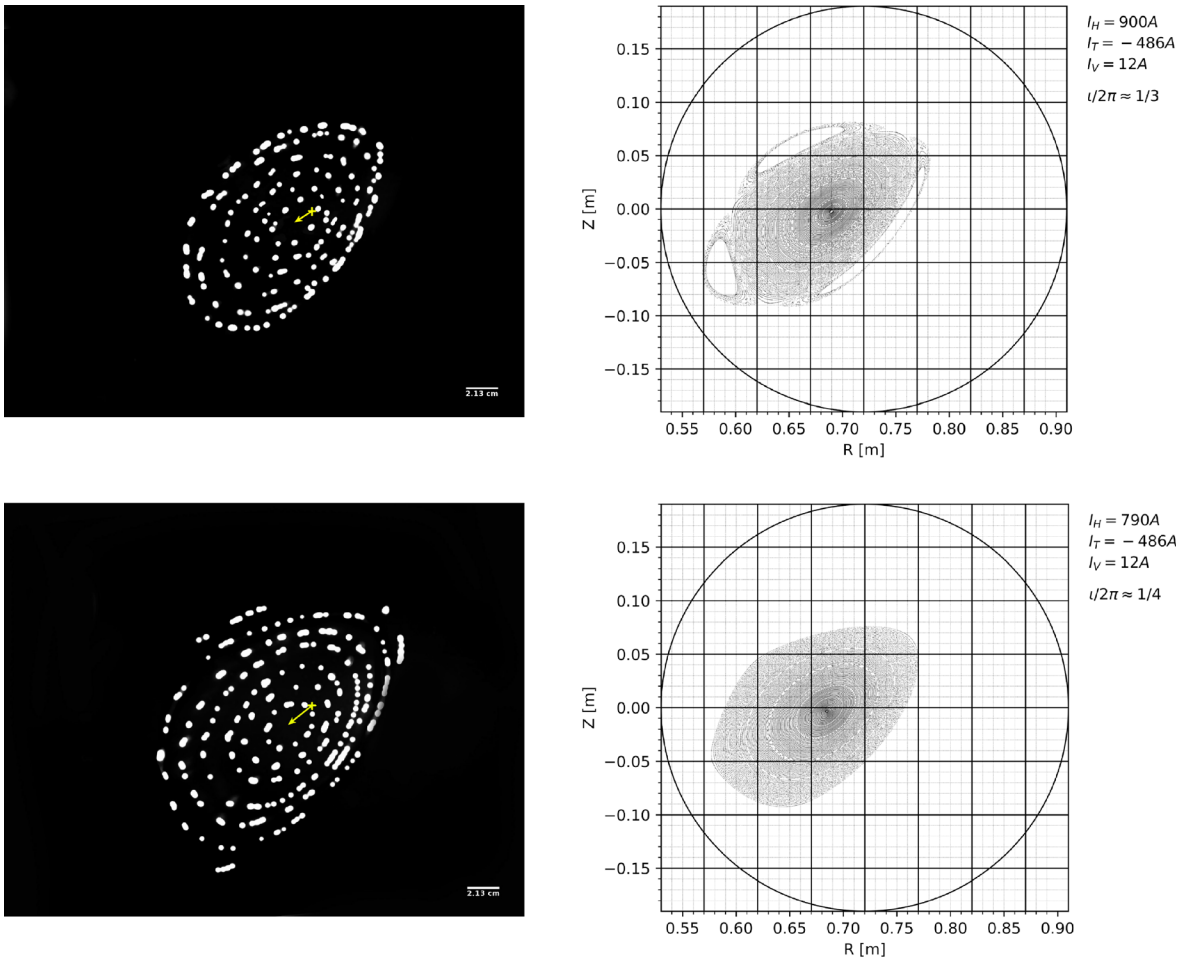

FIG. 6. Experimental (left) and computational (right) magnetic flux surfaces for $\iota \approx 1/3$ (top) and $\iota \approx 1/4$ (bottom) with a $+12$ A current through the vertical field coils. The arrow shows the magnetic axis displacement toward the high-field side with the cross indicating its position with no vertical field applied.

another before filtering, possibly caused by an additional misalignment of the CCD camera. This can explain why the experimentally found radial location of the magnetic axis was larger than the expected $R = 70.5$ cm. By having an angled view of the magnetic surfaces, the magnetic axis would come sooner than it should in the image from the low-field side, increasing its distance to the high-field sidewall.

Running a negative current through the vertical coils also resulted in the removal of the $n = 1$ non-natural islands and a shift of the magnetic axis, this time toward the low-field side. Whereas no islands were observed for the rotational transforms of $\approx$1/3 and $\approx$1/5, running this negative current resulted in the appearance of a 2/7 island chain when in the magnetic configuration of $\iota \approx 1/4$. This is the only occurrence where $n = 2$ islands were observed during this experimental campaign. The experimental and computational magnetic flux surfaces with the negative 12 A vertical coil current for $\iota \approx 1/4$ and $\iota \approx 1/5$ are shown in Fig. 7. While the experimentally generated image for the $\approx$1/4 rotational transform configuration does not properly resolve the 2/7 islands, these are clearly visible in the computational Poincaré surface which confirms the somehow particular shape of the flux surface in this case. The experimental $\iota \approx 1/5$ magnetic flux surface of Fig. 7 exhibits flatter magnetic surfaces in the edge region which are caused by the 1/4 islands located outside the measured domain as seen in the corresponding FIELDLINES Poincaré surface.

Polar plots of the magnetic surfaces for $\iota \approx 1/4$ are shown in Fig. 8 with all three vertical coil currents of 0 A, $+12$ A, and -12 A. The removal of the non-natural $n = 1$ islands for both the $+12$ A and -12 A vertical field coil current cases is easily noticeable in these plots. Similarly, the appearance of the 2/7 island chain with the negative vertical field coil current case is clearly seen.

C. Effect of the vertical field on the rotational transform

To understand what effect the vertical field has on the magnetic topology, it is useful to take a look at the evolution of the rotational transform along the magnetic surfaces with and without the presence of a vertical field. Figure 9 shows the radial profiles of the rotational

Published under license by AIP Publishing

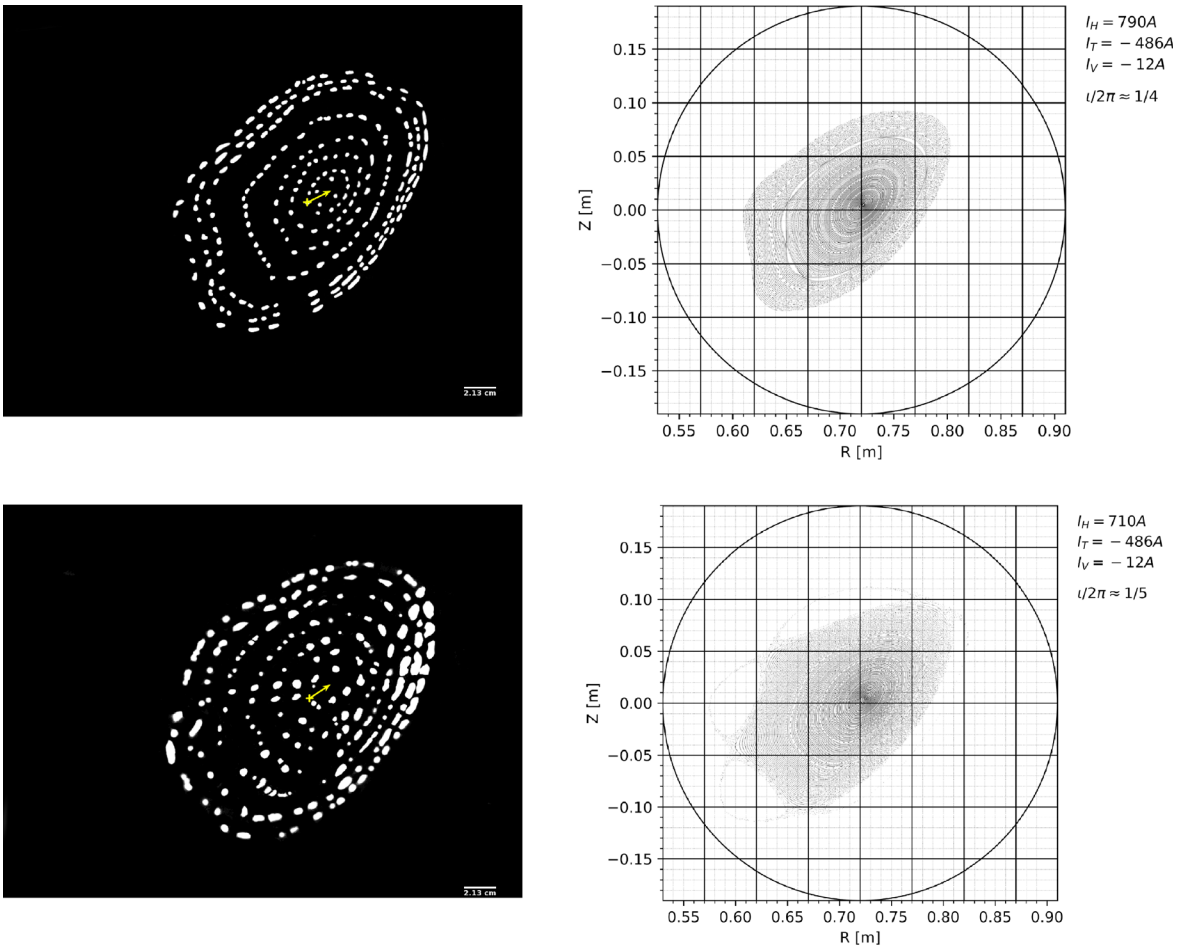

FIG. 7. Experimental (left) and computational (right) magnetic flux surfaces for $\iota \approx 1/4$ (top) and $\iota \approx 1/5$ (bottom) with a −12 A current through the vertical field coils. The magnetic axis displacement from its initial position indicated by the cross is traced by the arrow on the experimental images. A 2/7 island chain can be seen in the $\iota \approx 1/4$ configuration.

transform for the different cases studied. The application of a vertical field changes the value of the rotational transform at the magnetic axis, lowering it for a positive vertical field current and raising it for a negative current. As a result, the magnetic configuration moves to a regime where the $n = 1$ magnetic resonances can be avoided because these resonances are pushed out of confinement. The flatter magnetic surfaces in the outer regions of the flux surfaces in the negative vertical field case are the result of the non-natural islands existing just outside of the confinement area. The $\iota \approx 1/4$ and $\iota \approx 1/5$ profiles of Fig. 9 with a -12 A vertical field current approach the resonant surfaces of 1/3 and 1/4, respectively. With the non-natural islands just outside of the observed flux surfaces, the flatter outer edges are expected.

By applying a vertical field, the resonant position of the $n = 1$ error field along the magnetic flux surface is radially shifted. If in addition to the $n = 1$ error field, a higher order $n = 2$ field of sufficiently high amplitude exists, the island structure changes. Whereas the magnetic structure is generally dominated by the $n = 1$ error field for the various poloidal mode numbers studied, in the case of $\iota \approx 1/4$ with the negative 12 A vertical field coil current, the higher order $n = 2$ islands did show up. The corresponding rotational transform profile seen in Fig. 9 can be seen evolving very close to the 2/7 resonant surface. A closer look at the radial profile of the rotational transform in this case displayed in Fig. 10 shows the crossing of the 2/7 resonant surface at the exact location where the 2/7 islands are observed in the Poincaré section of Fig. 7. Another hint of potential $n = 2$ islands being present can be seen in the rotational transform profile for $\iota \approx 1/3$ with a negative 12 A vertical field current where at the very end, it seems to flatten as it approaches the 2/5 surface. This however was not observed experimentally as it occurs past the measured confined domain.

The reason why a 2/7 island chain does not show up in the $\iota \approx 1/3$ case with a positive vertical field current, even though the rotational transform clearly crosses the 2/7 surface, is that the magnetic structure is probably still dominated by the $n = 1$ error field in this case. The corresponding Poincaré section shown in Fig. 6 displays large 1/3 islands at the LCFS. As for the higher poloidal mode numbers of 9 and 11 for $n = 2$, respectively, reached in the $\iota \approx 1/4$ and $\iota \approx 1/5$ magnetic configurations with a positive

Published under license by AIP Publishing

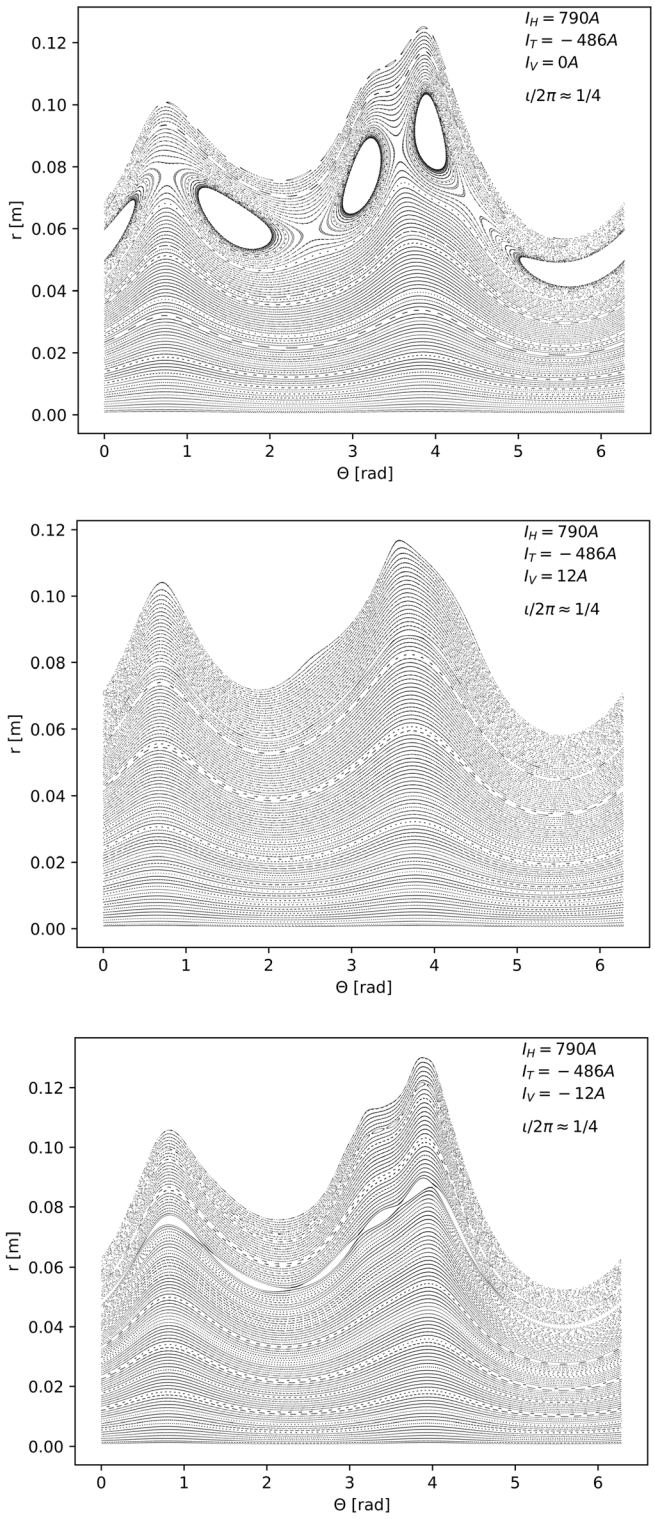

FIG. 8. Polar plots of the magnetic lines, for a rotational transform configuration of $\iota \approx 1/4$ with no vertical field (top), a $+12$ A vertical coil current (middle), and a -12 A vertical coil current (bottom).

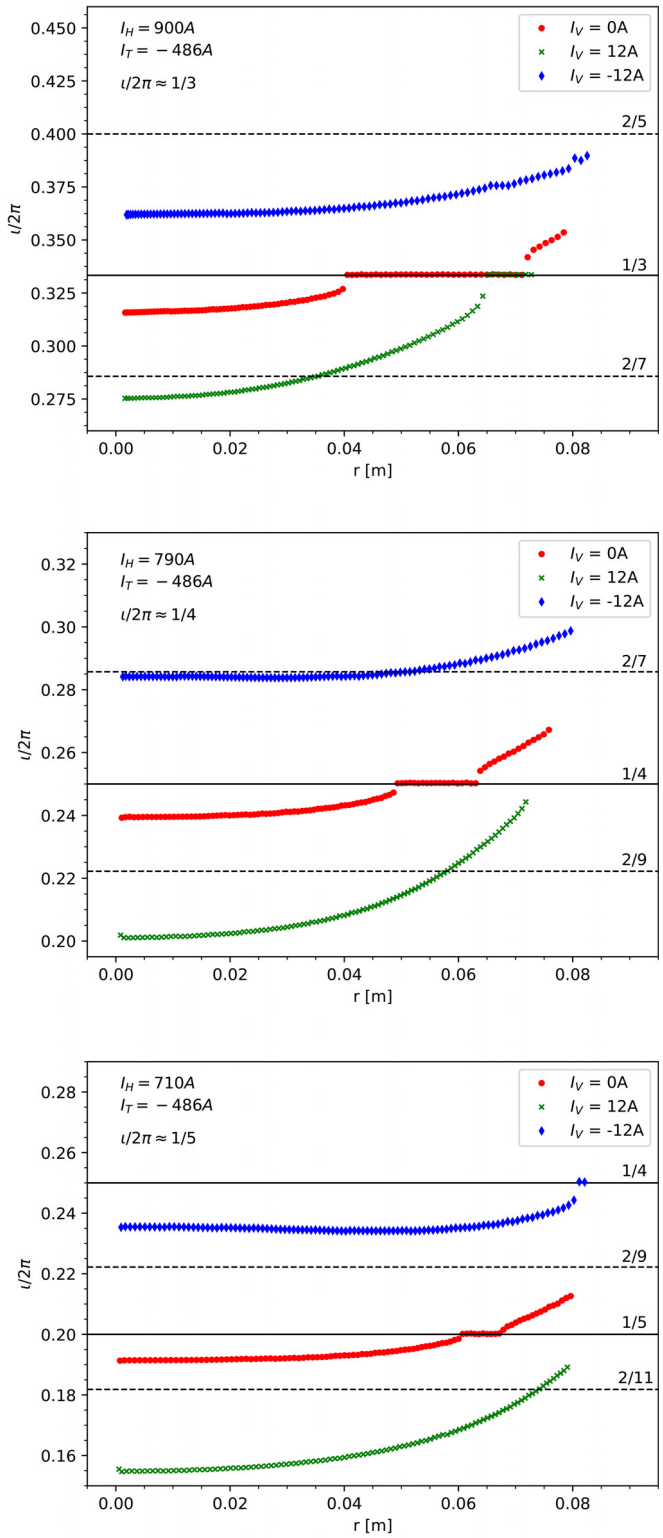

FIG. 9. Radial rotational transform profiles for $\iota \approx 1/3$ (top), $\iota \approx 1/4$ (middle), and $\iota \approx 1/5$ (bottom), with and without the presence of a vertical field.

Published under license by AIP Publishing

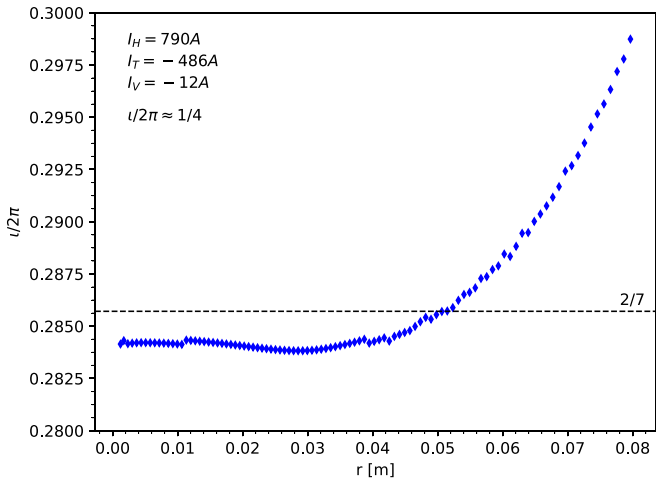

FIG. 10. Close-up of the radial rotational transform profile for $\iota \approx 1/4$ with a negative 12 A vertical field current.

vertical field current, a potential explanation as to why 2/9 and 2/11 islands were not detected has to do with the radial decay of these modes. Indeed, as discussed by Bozhenkov *et al.*,[19] modes with a poloidal mode number m see their amplitude decay as r^{m-1}. This decay is clearly noticeable in the Poincaré sections of Fig. 5 with the increasing poloidal mode number. If the amplitude of the $n = 2$ error field is not strong enough, the higher order 2/9 and 2/11 islands will be more difficult to form.

D. Application to PMI experiments

The location of the magnetic axis at the poloidal plane where the LiMIT and FLiLi plates and the HIDRA-MAT samples will be exposed to the HIDRA plasma is critical in designing the corresponding experimental setup. At $R \approx 70.5$ cm and $Z \approx 0$, there is enough room radially to make testing of small samples and the limiter configuration of LiMIT and FLiLi possible and enough room vertically for the divertor configuration of the plates. However, the dimension of the PFC cannot be too large, so that the whole experimental apparatus can fit inside the vacuum vessel without getting too close to the magnetic axis. Adding a vertical field, in addition to allowing operation in regimes with no low-order rational resonances, can help in creating additional space to comfortably carry out the experiments. Because of the negative direction of the toroidal field current, it is the positive vertical field current that shifts the magnetic axis toward the high-field side. Hence, a positive current through the vertical coils is desirable for PMI experiments on HIDRA as it creates extra room for installing the desired apparatus and necessary diagnostics. However, the vertical field does not only lead to the radial shifts of the magnetic axis but also moves it out of the horizontal $Z = 0$ plane. This shift, even if small, can impact the contact point between the plasma and tested PFC and should be taken into account when planning PMI experiments. The overall shift of the magnetic axis changes for the different magnetic configurations, with an average radial shift on the order of ≈ 2 cm and a vertical shift on the order of ≈ 4 mm. Applying a $+12$ A vertical field current in the low-field regime of HIDRA helps in radially pushing the plasma center from 20.5 cm away from the low-field sidewall to about 23 cm, giving additional space to maneuver and properly install the LiMIT and FLiLi plates in their limiter configuration along with their support structure. The magnetic mapping is also essential to gain knowledge of the behavior of the HIDRA magnetic structure in different operating conditions and the plasma position in the vacuum vessel. This is crucial so that the angle of the plates and/or samples is appropriately chosen to obtain proper contact with the plasma and successfully test and develop liquid lithium limiter and divertor concepts. A computer-aided design (CAD) of the LiMIT/FLiLi setup inside the vacuum vessel is shown in Fig. 11. In their current versions, the LiMIT and FLiLi plates are quite large for testing in a machine the size of HIDRA, with LiMIT currently measuring $32 \times 25\,\text{cm}^2$ and FLiLi measuring $32 \times 30\,\text{cm}^2$. Taking advantage of the ability to split HIDRA in half, installing such large components inside the vacuum vessel becomes possible. This is also needed for setting up the LiMIT/FLiLi apparatus with all the necessary diagnostics. For the LiMIT plate shown in Fig. 11, the addition of the vertical field pushes the magnetic axis away to a 4.5 cm normal distance from the PFC plate. Reducing the size of the plates is being considered to further increase the distance between the PFC and the magnetic axis. Too close of a distance between the two can effectively destroy the plasma. Moreover, decreasing the dimensions of the LiMIT and FLiLi plates in their upgraded designs for future HIDRA tests can facilitate the installation procedure inside the vacuum vessel and make the experiments more efficient and easier to carry out.

Another control over the magnetic structure that can be utilized consists in reversing the direction of the toroidal coil current. This will flip the orientation of the magnetic flux surface and change the plasma contact with the tested component. This could be desirable depending on the adopted design and final experimental setup to increase the contact region between the PFC and the plasma.

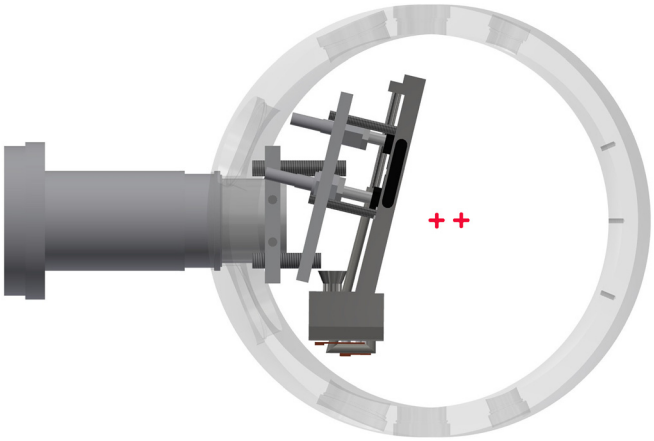

FIG. 11. CAD of the LiMIT plate in its limiter configuration with its support structure in the HIDRA vacuum vessel mounted from the low-field side. The crosses indicate the magnetic axis position with no vertical field (left cross) and $+12$ A vertical field current (right cross).

Published under license by AIP Publishing

IV. CONCLUSIONS

Mapping of the HIDRA magnetic flux surfaces was performed at two poloidal cross sections where the magnetic topology is identical to where the LiMIT and FLiLi plates will be installed and the HIDRA-MAT test samples exposed to the plasma. The magnetic surfaces were experimentally measured using the electron gun and fluorescent detector technique for several magnetic configurations, with and without the presence of a vertical field. The FIELDLINES code was used to follow the field lines inside the vacuum vessel, after which Poincaré sections were generated to obtain the computational magnetic surfaces. Comparing the experimental and computational images qualitatively gave good agreement between the two, confirming that the computational model accurately reproduced the physical system at hand. The measured experimental magnetic surfaces exhibited a similar dominant $n = 1$ error field as the one reported from previous WEGA campaigns. This error field was reproduced for HIDRA by adding a uniform horizontal 4 mm shift to the helix in the computational model, 1 mm larger than the one that was used to simulate the WEGA error field. The slight difference between the two error fields was expected because of the disassembly and reassembly of the machine when moving to CPMI. This confirmed that the error field originates from the physical device itself, probably caused by engineering imperfections and slight offsets among the different components and magnetic coils during assembly.

Applying a vertical field was shown to allow operation without the $n = 1$ order rational resonances and to shift the magnetic axis at the poloidal cross section of interest on the order of 2 cm radially and 3–4 mm vertically. It also revealed the presence of a higher order $n = 2$ error field, creating $n = 2$ islands in specific conditions. The addition of a vertical field gives an additional control over the magnetic structure of the HIDRA plasma and can be used to create extra space for the experimental setup for the planned PMI experiments on the machine.

Now that the experimental surfaces have been successfully mapped and compared to the Poincaré sections from the FIELDLINES code, a complete magnetic grid can be generated for HIDRA. This will allow particle and heat flux simulations to be performed, with experiments being planned to validate the computational model. After this, proper planning of PMI experiments will be possible, with a complete map of the HIDRA plasma and knowledge of the real heat and particle fluxes that the plates in the limiter and divertor regions will be subject to for the different operational regimes.

ACKNOWLEDGMENTS

The authors would like to thank Dr. Matthias Otte from IPP for his help and advices concerning the mapping of the HIDRA magnetic surfaces and Dr. Samuel Lazerson from PPPL for his help with the FIELDLINES code. This work was supported by the Department of Energy under No. DE-SC0016322 and the Princeton Plasma Physics Laboratory under No. DE-AC02-09CH11466, the Grainger College of Engineering, and the Department of Nuclear, Plasma and Radiological Engineering at UIUC.

REFERENCES

[1] R. Rizkallah, D. Andruczyk, A. Shone, D. Johnson, Z. Jeckell, S. Marcinko, Z. Song, D. Curreli, F. Bedoya, A. Kapat, J. P. Allain, M. Christenson, M. Szott, S. Stemmley, H. Sandefur, D. N. Ruzic, R. Maingi, J. Hu, G. Zuo, and J. Schmitt, "Latest results from the hybrid Illinois device for research and applications (HIDRA)," IEEE Trans. Plasma Sci. **46**, 2685–2690 (2018).

[2] J. Ren, J. S. Hu, G. Z. Zuo, Z. Sun, J. G. Li, D. N. Ruzic, and L. E. Zakharov, "First results of flowing liquid lithium limiter in HT-7," Phys. Scr. **T159**, 014033 (2014).

[3] D. Ruzic, W. Xu, D. Andruczyk, and M. Jaworski, "Lithium–metal infused trenches (LiMIT) for heat removal in fusion devices," Nucl. Fusion **51**, 102002 (2011).

[4] D. Ruzic, M. Szott, C. Sandoval, M. Christenson, P. Fiflis, S. Hammouti, K. Kalathiparambil, I. Shchelkanov, D. Andruczyk, R. Stubbers, C. J. Foster, and B. Jurczyk, "Flowing liquid lithium plasma-facing components—Physics, technology and system analysis of the LiMIT system," in Proceedings of the 22nd International Conference on Plasma Surface Interactions 2016, 22nd PSI [Nucl. Mater. Energy **12**, 1324–1329 (2017)].

[5] W. Xu, D. Curreli, D. Andruczyk, T. Mui, R. Switts, and D. Ruzic, "Heat transfer of TEMHD driven lithium flow in stainless steel trenches," in Proceedings of the 20th International Conference on Plasma-Surface Interactions in Controlled Fusion Devices [J. Nucl. Mater. **438**, S422–S425 (2013)].

[6] J. Hu, G. Zuo, J. Ren, Q. Yang, Z. Chen, H. Xu, L. Zakharov, R. Maingi, C. Gentile, X. Meng, Z. Sun, W. Xu, Y. Chen, D. Fan, N. Yan, Y. Duan, Z. Yang, H. Zhao, Y. Song, X. Zhang, B. Wan, J. G. Li, and EAST Team, "First results of the use of a continuously flowing lithium limiter in high performance discharges in the EAST device," Nucl. Fusion **56**, 046011 (2016).

[7] G. Z. Zuo, J. S. Hu, R. Maingi, Q. X. Yang, Z. Sun, M. Huang, Y. Chen, X. L. Yuan, X. C. Meng, W. Xu, C. Gentile, A. Carpe, A. Diallo, R. Lunsford, D. Mansfield, T. Osborne, K. Tritz, and J. G. Li, "Upgraded flowing liquid lithium limiter for improving Li coverage uniformity and erosion resistance in east device," Rev. Sci. Instrum. **88**, 123506 (2017).

[8] M. Otte, J. Lingertat, and F. Wagner, "Magnetic flux surface measurements with vertical field and compensation coils at the WEGA stellarator," in *Proc. 14th Int. Stellarator Workshop* (Greifswald, Germany, 2003).

[9] S. A. Lazerson, M. Otte, S. Bozhenkov, C. Biedermann, T. S. Pedersen, and W7-X Team, "First measurements of error fields on W7-X using flux surface mapping," Nucl. Fusion **56**, 106005 (2016).

[10] S. A. Lazerson, M. Otte, M. Jakubowski, B. Israeli, G. A. Wurden, U. Wenzel, T. Andreeva, S. Bozhenkov, C. Biedermann, G. Kocsis, T. Szepesi, J. Geiger, T. S. Pedersen, D. Gates, and W7-X Team, "Error field measurement, correction and heat flux balancing on Wendelstein 7-X," Nucl. Fusion **57**, 046026 (2017).

[11] D. Spong, S. Hirshman, J. Whitson, D. Batchelor, R. Sanchez, B. Carreras, V. Lynch, J. Lyon, P. Valanju, W. Miner, P. Moroz, M. Zarnstorff, D. Monticello, A. Ware, and L. Garcia, "Design studies of low aspect ratio quasi-omnigenous stellarators," Nucl. Fusion **40**, 563–567 (2000).

[12] S. P. Hirshman, D. A. Spong, J. C. Whitson, V. E. Lynch, D. B. Batchelor, B. A. Carreras, and J. A. Rome, "Transport optimization and MHD stability of a small aspect ratio toroidal hybrid stellarator," Phys. Rev. Lett. **80**, 528–531 (1998).

[13] P. Drewelow, T. Bräuer, M. Otte, F. Wagner, and A. Werner, "Three-dimensional photogrammetric measurement of magnetic field lines in the WEGA stellarator," Rev. Sci. Instrum. **80**, 123501 (2009).

[14] M. Otte, H. Laqua, E. Chlechowitz, P. Drewelow, M. Glaubitz, S. Marsen, E. Müller, Y. Podoba, J. Schacht, T. Stange, F. Steffen, F. Wagner, R. Wolf, and D. Zhang, "Overview of experimental results from the WEGA stellarator," Contrib. Plasma Phys. **50**, 780–784 (2010).

[15] M. Otte and J. Lingertat, "Initial results of magnetic surface mapping in the WEGA stellarator," in 29th European Physical Society Conference on Plasma Physics and Controlled Fusion. Contributed Papers of European Physical Society, edited by R. Behn and C. Varandas (2002).

[16] J. P. Freidberg, "MHD—Macroscopic equilibrium," in *Plasma Physics and Fusion Energy* (Cambridge University Press, 2007), pp. 245–295.

[17] J. Wesson, *Tokamaks*, International Series of Monographs on Physics Series (Oxford University Press, 2011), p. 40.

[18] F. F. Chen, *Introduction to Plasma Physics and Controlled Fusion* (Springer International Publishing, 2016), pp. 26–29.

[19] S. Bozhenkov, S. Lazerson, M. Otte, D. Gates, T. S. Pedersen, and R. Wolf, "Methods for measuring 1/1 error field in Wendelstein 7-X stellarator," Nucl. Fusion **56**, 076002 (2016).

Published under license by AIP Publishing